

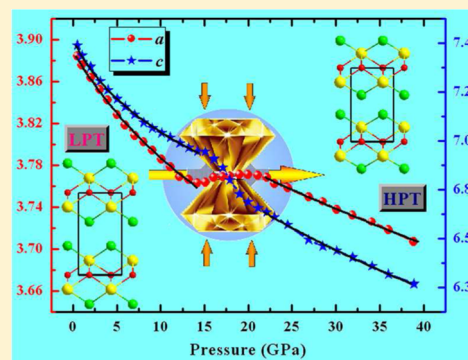
HPSTAR
141-2016

Isostructural Phase Transition in Bismuth Oxide Chloride Induced by Redistribution of Charge under High Pressure

Jinggeng Zhao,^{*,†} Lingling Xu,[‡] Yang Liu,[‡] Zhenhai Yu,[§] Chunyu Li,[§] Yi Wang,^{*,†} and Zhiguo Liu^{*,#}[†]Natural Science Research Center, Academy of Fundamental and Interdisciplinary Sciences, and [#]Department of Physics, Harbin Institute of Technology, Harbin 150080, China[‡]Key Laboratory of Photonic and Electric Bandgap Materials, Ministry of Education, School of Physics and Electronic Engineering, Harbin Normal University, Harbin 150025, China[§]Center for High Pressure Science and Technology Advanced Research, Shanghai, 201203, China

Supporting Information

ABSTRACT: As one of important semiconductor photocatalysts, bismuth oxide chloride (BiOCl) crystallizes into a tetragonal matlockite structure with the space group of $P4/nmm$. In this work, the in situ high-pressure angle-dispersive X-ray diffraction experiments and the first-principle calculations were performed on BiOCl, in order to explore the crystal and electronic structure evolution processes upon compression. At 15.1 GPa, BiOCl undergoes a tetragonal to tetragonal isostructural phase transition and then completely transforms into a high-pressure tetragonal phase at 22.1 GPa, which adopts the same crystal structure as that of the low-pressure tetragonal phase. According to the ab initio calculation results, the redistribution of Bader charge between the Bi, O, Cl ions under high pressure induces the isostructural phase transition in BiOCl and causes the different electronic structures between the high-pressure and low-pressure phases. The pressure-induced crystal and electronic structure changes in BiOCl could be a reference to explain the mechanism of isostructural phase transition in other similar compounds upon compression.



INTRODUCTION

In the past few years, semiconductor photocatalysts have received a lot of attention for potential environment and energy applications.¹ Among the efficient photocatalysts, bismuth oxyhalides BiOCl, BiOBr, and BiOI show high photocatalytic activity because of the Bi³⁺ with s^2 configuration and the layer crystal structure.^{2–11} Due to the unique crystal structure and excellent electronic and optical properties, they could be applied in many important and promising fields, e.g., pigments in the cosmetic industry, magnetic materials, gas sensors, phosphor, pharmaceuticals, and catalysts in the oxidative coupling of methane.^{2–11} BiOCl, BiOBr, and BiOI present indirect band gaps, with a band gap width (E_g) of 1.57–3.504 and 1.77–3.5 eV obtained from the calculation^{12–14} and experiment^{4–7} data, respectively. However, the sister compound BiOF presents a direct or indirect band gap corresponding to the calculation results with or without the Bi 5d states.¹² It is important to investigate the structure evolution of these compounds because it could modulate the physical properties. At ambient conditions, BiOX (X = F, Cl, Br, and I) adopts the tetragonal matlockite (PbFCl) structure with the space group of $P4/nmm$, in which the Bi, O, and X ions occupy the $2c$ (0.25, 0.25, z_{Bi}), $2a$ (0.25, 0.75, 0), and $2c$ (0.25, 0.25, z_{X}) Wyckoff positions, respectively.^{15–18}

Among the bismuth oxyhalides, BiOCl was the first material to be used as a photocatalyst and could be synthesized by using

a low temperature wet-chemical method.^{2–6} Figure 1 shows the schematic view of crystal structure of BiOCl at ambient conditions. The structure of BiOCl is similar to that of the 111-type iron-based superconductors AFeAs (A = Li, Na), which adopt the antimatlockite structure possessing the space group of $P4/nmm$.^{19–21} Compared with another 1111-type iron-based superconductors Ln(O_{1-x}F_x)FeAs (Ln = lanthanide elements),^{22–26} there is no metal ion in the center of the Cl₄ tetragonal in BiOCl. In the crystal structure of BiOCl at ambient conditions, the Bi ion is eight-coordinated by four O and four Cl ions that forms a Bi[O₄Cl₄] decahedron, as shown in Figure 1. The surface of Bi[O₄Cl₄] decahedron is composed of one Cl₄ square, one O₄ square, four O₂Cl triangles, and four OCl₂ triangles. In BiOCl, the Bi, O, and Cl ions form a Bi–O–Cl layer (Cl–Bi–O₂–Bi–Cl) stacking along the c -axis.

Pressure has played an important role in modulating the crystal structure on the iron-based superconductors and related parent compounds, e.g. 1111-type Ln(O,F)FeAs (Ln = Nd, Ce),^{27,28} 122-type AFe₂As₂ (A = Ca, Sr, Ba, Eu),^{29–35} and 111-type Na_{1-x}FeAs.³⁶ Under high pressure, these materials undergo a tetragonal to tetragonal isostructural phase transition, in which the high-pressure phase keeps the same

Received: July 24, 2015

Revised: November 12, 2015

Published: November 13, 2015

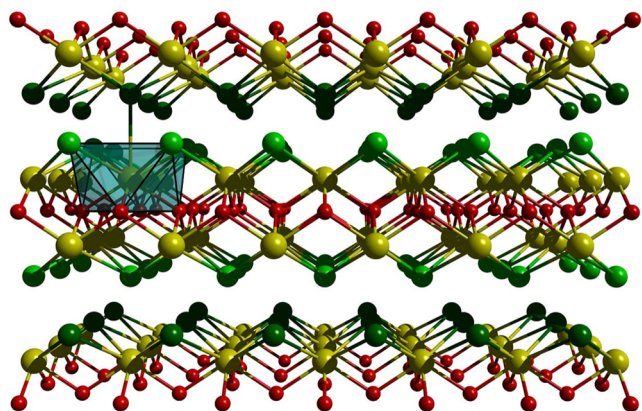


Figure 1. Schematic views of crystal structure of BiOCl, as well as one Bi[O₄Cl₄] decahedron. The yellow, red, and green globes represent the Bi, O, and Cl atoms, respectively. The *a*-, *b*-, and *c*-axes are perpendicular to the plane, horizontal in the plane, and vertical in the plane, respectively.

space group as that of the low-pressure phase.^{27–36} Considering the similar structure to the iron-based superconductors, high pressure could also affect the crystal structure of BiOCl. On the other hand, previous investigations showed that the pressure-induced structure phase transition and insulator-to-metal transition exist in TiOCl, which crystallizes into an orthorhombic with the space group of *Pmmm*, obtained from calculation³⁷ and experiment^{38–41} results. At about 10.5 GPa, TiOCl transforms into a monoclinic phase (space group: *P2₁/m*), with a spin-Peierls to Peierls transition induced by the Ti–Ti dimerization under high pressure.³⁸ Due to the similarity in chemical content to TiOCl, the structure and physical properties of BiOCl may also be modulated by pressure. Therefore, it is important to perform the corresponding high-pressure experiments on BiOCl, in order to investigate the effect of pressure on the crystal and electronic structure evolution processes.

In this work, by using a diamond anvil cell (DAC) technique combined with an in situ angle-dispersive synchrotron X-ray diffraction (AD-XRD) experimental method, a pressure-induced tetragonal to tetragonal isostructural phase transition on photocatalytic material BiOCl at 15.1 GPa was found. The ab initio calculations were also performed by using the density functional theory (DFT), which indicated that the redistribution of Bader charge between the Bi, O, Cl ions under high pressure causes the isostructural phase transition in BiOCl.

EXPERIMENTAL AND COMPUTATIONAL METHODS

The BiOCl sample used in this work was prepared via a coprecipitation method by using the bismuth nitrate (Bi(NO₃)₃·5H₂O) and potassium chloride (KCl), and the cetyltrimethylammonium bromide (CTAB) as the raw materials and template, respectively. The synthesized compound crystallizes into a pure phase, detected by the XRD pattern. The in situ high-pressure AD-XRD experiments on BiOCl were performed at room temperature at the BL15U1 beamline of the Shanghai Synchrotron Radiation Facility (SSRF), and the X17C beamline of the National Synchrotron Light Source (NSLS), Brookhaven National Laboratory, using a monochromatic X-ray beam with the incident wavelength of 0.6199 and 0.4067 Å, respectively. The incident X-ray

monochromatic beam was slit-collimated down to $5 \times 3 \mu\text{m}^2$ at BL15U1 beamline of SSRF. In the high-pressure experiments, the symmetry diamond anvil cells maintain the rectangular slit in the emergent direction, with a diameter of 500 or 300 μm of the flat culets in the diamonds. The sample was prepressed to a pellet with thickness about 10–15 μm and then loaded into the sample chamber of 100–160 μm diameter. The sample chamber was drilled in the T301 stainless steel gasket preindented to 40–55 μm thickness. The ruby luminescence method was used to measure pressure around the sample in the chamber.⁴² Silicone oil or methanol–ethanol (4:1) mixture, which could ensure a quasi-hydrostatic pressure environment,^{43–47} were used as the pressure-transmitting medium. Two-dimensional diffraction patterns were collected on a charge-coupled device (CCD) detector. The CeO₂ standard was used to calibrate the distance between sample and detector and the orientation parameters of the detector. The recorded images were integrated using the program Fit2D.⁴⁸ The high-pressure XRD patterns are refined by using the Rietveld methods.⁴⁹ The crystal structure were analyzed by using the General Structure Analysis System (GSAS)^{50,51} and PowderCell⁵² program packages.

The first-principle calculations based on the density functional theory were performed to explore the influence of high pressure on the electronic structures of BiOCl. Spin–orbit coupling interactions were included in the electronic structure calculations due to the large atomic mass of Bi. The Bi 5d states were also considered in all the calculations. Bader analysis on the charge density grids was performed by adopting an improved algorithm⁵³ and using the projector augmented plane-wave (PAW) method implemented in the Vienna ab initio simulation package (VASP).^{54,55} The kinetic energy cutoff for the plane-wave basis sets used in the Perdew–Burke–Ernzerhof (PBE) parametrization of the general gradient approximation (GGA)⁵⁶ calculations was chosen to be 520 eV. The positions of atoms were fully relaxed until the residual Hellmann–Feynman forces fell below 0.01 eV/Å. The electronic band structure and density of states (DOS) calculations for BiOCl were carried out using WIEN2K software within the PBE-GGA.⁵⁶ The plane-wave cutoff was defined by $RK_{\text{max}} = 9.5$. Convergence test gave the choices of 2000 and 10000 *k* points in the full Brillouin zone (BZ) for the self-consistent and DOS calculations, respectively. The band structures of BiOCl were calculated along the special lines connecting the high-symmetry points: Γ (0, 0, 0), Z (0, 0, 0.5), X (0, 0.5, 0), M (0.5, 0.5, 0), R (0, 0.5, 0.5), and A (0.5, 0.5, 0.5) in the *k*-space.

RESULTS AND DISCUSSION

All the XRD patterns of BiOCl up to 38.9 GPa at room temperature collected at BL15U1 beamline of SSRF are shown in Figure S1 of the Supporting Information, and the representative XRD patterns under different pressures are plotted in Figure 2a, without any new peaks observed in the experimental pressure range. However, the pressure dependence of several peaks begin to abnormal at above 15.1 GPa. Figure 2b shows the detailed evolutions of peak (112) and (200) for BiOCl in the pressure range of 12.2 to 24.5 GPa, in which the bold lines are a guide for the eyes. The peak (200) begins to shift to the low-angle direction from 15.1 GPa with the increasing pressure and then normally moves to the high-angle direction when pressure is larger than 22.1 GPa. In the experimental pressure range, the peak (112) shifts to the high-

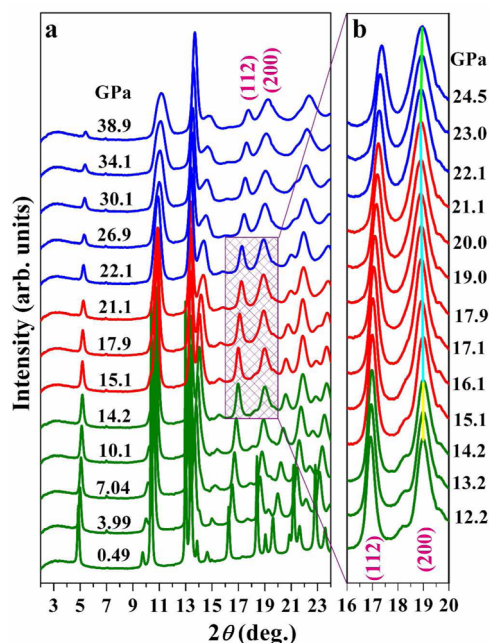


Figure 2. (a). Spectra of angle-dispersive X-ray diffraction (AD-XRD) patterns of BiOCl at room temperature up to 38.9 GPa ($\lambda = 0.6199$ Å). (b). Detailed evolution of peaks (112) and (200) in the pressure range of 12.2 to 24.5 GPa.

angle direction upon compression. Figure 3 shows the pressure dependences of d -spacing of peak (112) and (200). The d -

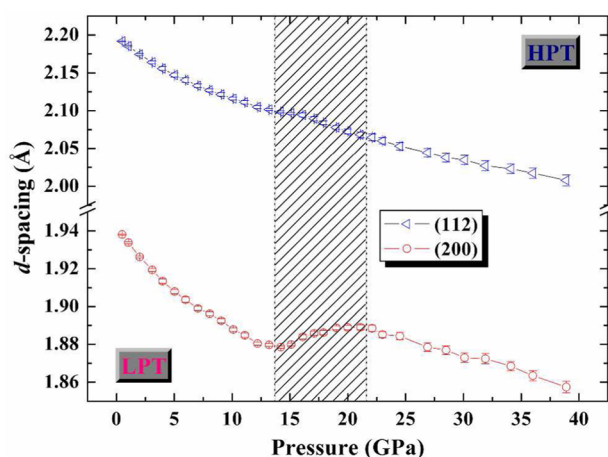


Figure 3. Pressure dependences of d -spacing of peak (112) and (200) of BiOCl up to 38.9 GPa.

spacing of peak (112) decreases with increasing pressure, while that of peak (200) increases first in the pressure range of 15.1 to 21.1 GPa and then starts to decrease at above 22.1 GPa. Therefore, according to the relationships of d -spacing versus pressure for these two peaks, a novel structural phase transition starts from 15.1 GPa and completes after 22.1 GPa in BiOCl. The experimental results are consistent with those obtained at X17C beamline of NSLS. When the pressure was released to ambient, BiOCl recovers to the low-pressure phase obtained from the XRD pattern, so the structural phase transition under high pressure is reversible.

By using Le Bail refinements based on previous reported unit cell,¹⁶ the pressure dependences of lattice parameters of BiOCl

are obtained, as shown in Figure 4a. Below 14.1 GPa, both the a - and c -axes shrink upon compression. From 15.1 GPa, the

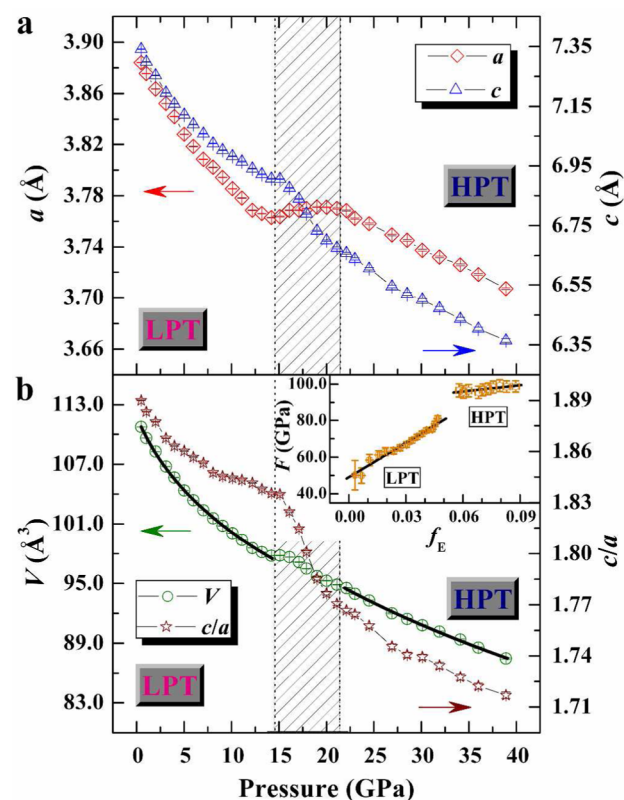


Figure 4. Pressure dependences of (a) lattice parameters, and (b) unit cell volume (V) and the c to a ratio (c/a) of BiOCl up to 38.9 GPa. The solid lines in V - P relationship are the fitting results according to the Birch–Murnaghan equation of state (BM-EoS). The inset in b shows the normalized pressure vs Eulerian strain (f_E - F) plot.

value of a -axis begins to increase, and the c -axis shrinks drastically in the pressure range of 15.1 to 21.1 GPa. At pressures above 22.1 GPa, both the values of a - and c -axes decrease. The abnormal pressure dependences of a - and c -axes indicate an isostructural phase transition starting at 15.1 GPa. Then BiOCl transforms completely into a high-pressure tetragonal (HPT) structure from 22.1 GPa, which keeps the same space group $P4/nmm$ as that of the primary low-pressure tetragonal (LPT) phase. The HPT phase at 22.1 GPa has a larger a -axis and smaller c -axis than those of the LPT phase at 14.2 GPa. The relationship of c to a ratio (c/a) versus pressure could distinctly reflect the isostructural phase transition process, as shown in Figure 4b. The value of c/a decreases with increasing pressure and goes through a drastic drop between 15.1 and 21.1 GPa. When BiOCl transforms into the HPT phase after 22.1 GPa, the c/a starts to become flatter than that in the pressure range of 15.1 to 21.1 GPa.

Figure 4b also shows the relationship of unit cell volume (V) versus pressure for BiOCl, in which the solid lines are the fitting results for the LPT and HPT phases, by using the third-order Birch–Murnaghan equation of state (BM-EoS).⁵⁷ The ambient-pressure isothermal bulk modulus B_0 is estimated as 48(1) and 89(3) GPa for the LPT and HPT phases, with a first-order pressure derivative B'_0 of 13 and 4.8, respectively. The fitted ambient unit cell volumes (V_0) of these two phases are equal to 111.81(16) and 111.5(4) Å³, respectively. Therefore,

the pressure range of 15.1 to 21.1 GPa represents a transitional region between the LPT and HPT phases, in which the pressure dependences of lattice parameters and unit cell volume are discontinuous. The f_E - F curves for the LPT and HPT phases are shown in the inset of Figure 4b, in which the f_E and F denote Eulerian strain and normalized pressure, respectively.^{58,59} The linear fitting to the f_E - F curves give a B_0 of 49(2) and 89(8) GPa for the LPT and HPT phases, with a B'_0 of 12.5(9) and 4.9(9), respectively, which are consistent with those obtained from the BM-EOS fit to the experimental data. The fit to the LPT phase leads to an unusual large B'_0 of 13, which indicates a strong increasing bulk modulus as pressure increases. Therefore, due to the slight turning point at about 7.04 GPa in the relationship of c/a versus pressure, two different pressure ranges below and above 7.04 GPa are used to fit the V - P relationship of the LPT phase of BiOCl. With a B'_0 of 9, the B_0 is estimated as 55.5(8) and 73(4) GPa in these two pressure ranges, respectively. The linear fitting to the f_E - F curves give a B_0 of 55(2) and 74(3) GPa in these two pressure ranges, with a B'_0 of 9.5(2.0) and 8.7(1.9), respectively, which are consistent with those obtained from the BM-EOS fit to the experimental data. Compared with the large transform of lattice parameters from 15.1 GPa, the change of c/a at 7.04 GPa is small, so the structure below 14.2 GPa is still denoted as the LPT phase. The axial compressibilities could reflect the anisotropy of axes upon compression.^{60,61} For the different axes, the axial bulk moduli could be obtained with a "linearized" BM-EoS by substituting the cube of the lattice parameter for the volume.^{58,59} With a B'_0 of 9, the axial bulk moduli $B_0(a)$ and $B_0(c)$ of the LPT phase below 7.04 GPa are equal to 81(2) and 30.3(5) GPa for the a - and c -axes, respectively. The compressibilities β_a and β_c , which could be obtained from the reciprocal value of three times $B_0(a)$ and $B_0(c)$,^{58,59} are equal to 0.0041(1) and 0.0110(2) GPa⁻¹, respectively. So it is easier to compress the c -axis than the ab -plane, due to the interspaces between the neighboring Bi-O-Cl layers along the c -axis.

The XRD patterns of BiOCl below 34.1 GPa are refined by using the Rietveld method.⁴⁹ The typical experimental (open circle) and fitted (line) results at 3.99, 14.2, 17.9, and 22.1 GPa are shown in Figure S2 of the Supporting Information, and the atomic coordination parameters at different pressures are summarized in Table S1 of the Supporting Information. The schematic views of crystal structure evolution of BiOCl upon compression are presented in Figure S3 of the Supporting Information. Figure 5 plots the pressure dependences of selected bond distances and angles, in which the bold lines are a guide for the eyes. The Bi-O distance decreases with increasing pressure, with the discontinuous evolution in the pressure range of 15.1 to 21.1 GPa. The Bi-Cl(I) and Bi-Cl(II) distances represent the distances between Bi and Cl ions in one Bi-O-Cl layer and two neighboring Bi-O-Cl layers along the c -axis, respectively, as shown in Figure 1. The Bi-Cl(I) and Bi-Cl(II) distances decrease with increasing pressure for the LPT phase, and increase slightly at 15.1 GPa. Then they begin to decrease up to 34.1 GPa, with a turning point at 22.1 GPa. The shrinkage of the Bi-Cl(II) distance upon compression is larger than that of Bi-Cl(I) distance. At 34.1 GPa, the Bi-Cl(II) distance is almost equal to the Bi-Cl(I) distance. The increase of the bulk modulus of the high-pressure phase in BiOCl is mainly due to the shrinkage of the Bi-Cl(II) distance between the two neighboring Bi-O-Cl layers upon compression. The O-Bi-O angle decreases with increasing pressure for the LPT phase and then increases in the

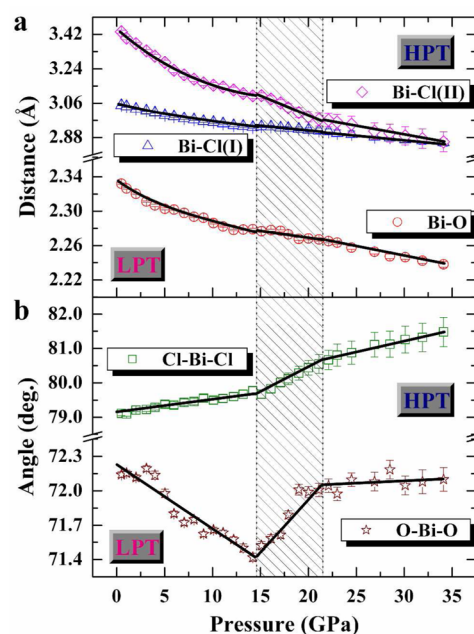


Figure 5. Pressure dependences of bond (a) distances and (b) angles for BiOCl up to 34.1 GPa. The bold lines are a guide for the eyes.

transitional region of 15.1–21.1 GPa. When BiOCl transforms into the HPT phase, the O-Bi-O angle almost does not change with increasing pressure. The Cl-Bi-Cl angle increases up to 34.1 GPa, with a discontinuous change in the transitional region. Therefore, all the main bond distances and angles of BiOCl undergo abnormal evolution when the isostructural phase transition has happened, which indicates that the crystal structure evolution process upon compression of the HPT phase is different from that of the LPT phase.

Generally, pressure can shrink the volume of a crystal lattice, which causes an effect similar to substituting the smaller ion in materials. For BiOX, the structural parameters are related closely to the X ionic radius (r_X), so the structure evolution of BiOX with decreasing r_X could be viewed as a comparison with the compression behavior of BiOCl. Figure S4a–d of the Supporting Information summarizes the relationships of crystal structural parameters, including a , c , V , c/a , and bond distances and angles, versus the decreasing r_X for BiOX, where the data are adopted according to refs 15–18. In Figure S4 of the Supporting Information, the X ionic radius are obtained from Shannon table,⁶² by assuming a -1 valence of X ions. Except for the X-Bi-X angle, the other structural parameters decrease when X goes from I to F ions. So the structure evolution with increasing pressure for the LPT phase of BiOCl is similar to that with decreasing r_X in BiOX. At pressure above 15.1 GPa, the structural parameters exhibit discontinuous pressure dependences, which indicates that the structure evolution with increasing pressure for the HPT phase of BiOCl is different from that with decreasing r_X in BiOX.

In general, the pressure-induced isostructural phase transition is related to the electronic structure change,^{63,64} so the theoretical calculations are important to obtain the mechanism of structure evolution upon compression in BiOCl. The ab initio calculations for BiOCl are performed up to 34.1 GPa to investigate the effect of electronic structure on the crystal lattice under high pressure, in which the structural parameters were directly obtained from the experimental results, with relaxing the atomic coordination parameters. Figure 6 shows the

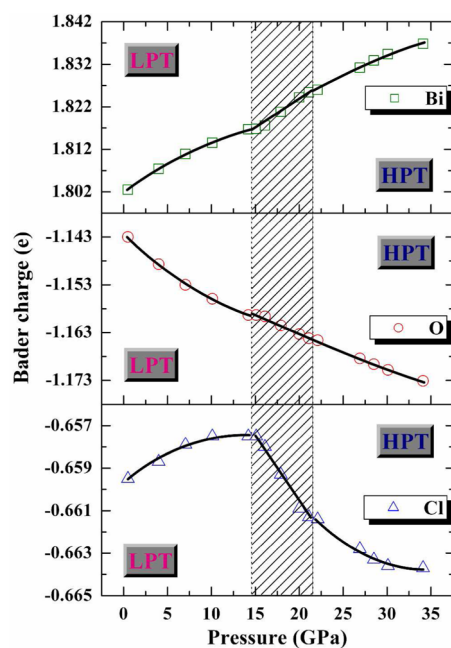


Figure 6. Pressure dependences of Bader charge of Bi, O, and Cl ions for BiOCl. The bold lines are a guide for the eyes.

pressure dependences of Bader charge of Bi, O, and Cl ions, with the bold lines as a guide for the eyes. In the LPT phase, with increasing pressure, the Bader charges of Bi and Cl ions increase and that of O ion decreases, which shows a negative charge transfer from Bi and Cl ions to O ion. At above 15.1 GPa, the Bader charge of Cl ion begins to decrease with increasing pressure, and Bi and O ions keep the same evolution as those in the LPT phase. So the charge transfer happens from Bi ion to O and Cl ions from this pressure. When BiOCl transforms into the HPT phase at 22.1 GPa, the Bader charge of Bi ion increases and those of O and Cl ions decrease, which show the discontinuous changes for those in the pressure range of 15.1 to 21.1 GPa. According to the relationships of Bader charge versus pressure, the charge transfer route between the three ions starts to change at 15.1 and 22.1 GPa. The discontinuity in the change of Bader charges upon compression indicates discontinuous changes for the configuration of bonding electrons, the interaction among bonding atoms, the bond strength, the bond length, and therefore the lattice parameters. So the redistribution of Bader charge results in the isostructural phase transition of BiOCl under high pressure, which is similar to that in the high-pressure structural evolutions of BiMn_2O_5 and Sb_2Te_3 .^{63,64}

The crystal structural phase transition of BiOCl induced by the redistribution of Bader charge would cause a change in electronic structure, so the energy band and DOS calculations including the Bi 5d states were performed up to 34.1 GPa. Figure 7a summarizes the highest valence bands and lowest conduction bands around the Fermi energy (E_F) at different pressures along the high-symmetry path (Z–A–M– Γ –Z–R–X– Γ), because they can display the pressure-dependent valence band maximum (VBM) and conduction band minimum (CBM), respectively. In Figure 7a, the CBM of BiOCl is almost maintained at the Z point in the first Brillouin zone, with a variable value at different pressures, and the VBM shifts to Z point along the R–Z path with increasing pressure. So the band gap of BiOCl presents indirectly in the whole range of

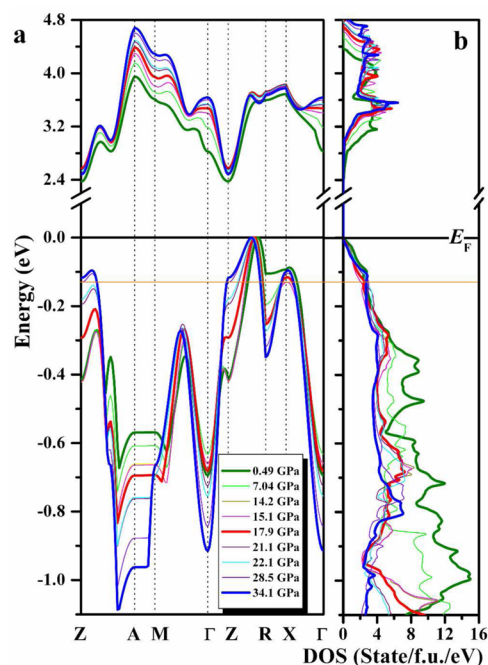


Figure 7. (a) Highest valence bands and lowest conduction bands, and (b) calculated total density of states (TDOS) around the Fermi energy (E_F) of BiOCl at different pressures. The orange line indicates a hypothetical Fermi energy (E'_F) of -0.13 eV.

loading pressure and tends to become direct due to the movement to Z point for the VBM along the R–Z path. The shift of VBM in the R–Z path under high pressure in BiOCl is similar to that with decreasing r_X in BiOX .^{12–14} Furthermore, the band structures in the energy range of -20 to 15 eV at 0.49, 17.9, and 34.1 GPa of BiOCl are shown in Figure S5 of the Supporting Information. The energy band widths increase with increasing pressure, due to the shrinkage of unit cell volume upon compression. When pressure is larger than 28.5 GPa, the gap at about -6 eV in the valence band begins to disappear, which results in a combination of energy bands on either side of that gap. A similar case exists also in the gap at about -16 eV at pressures above 28.5 GPa.

Figure 7b presents the TDOS around E_F at different pressures of BiOCl, which shows the complex relationship of TDOS versus pressure. Figure S6 of the Supporting Information shows the total and partial density of states (TDOS and PDOS) in the energy range of -20 to 15 eV at 0.49, 17.9, and 34.1 GPa. From the PDOS at different pressures, the Bi 6p state dominates the conduction band, and the O 2p, Cl 3p, and Bi 6s states contribute mainly to the valence band. At above 28.5 GPa, the combination of energy bands at about -6 eV is caused by the overlap of Bi 6s and 6p states, which may be related to the change of charge transfer between Bi and other ions. In Figure 6, the relationship of Bader charge versus pressure for Cl ion tends to become flat from 28.5 GPa, due to the redistribution of charge between Bi and Cl ions induced by the crossover of Bi electronic states upon compression.

Figure 8 shows the pressure dependence of band gap width (E_g), which could be obtained from the previous band structure and DOS data, and could reflect the relative movement between CBM and VBM in the band structure. The value of E_g is smaller than the previous calculation results,^{12–14} because the spin–orbit coupling interactions in Bi ion were considered in

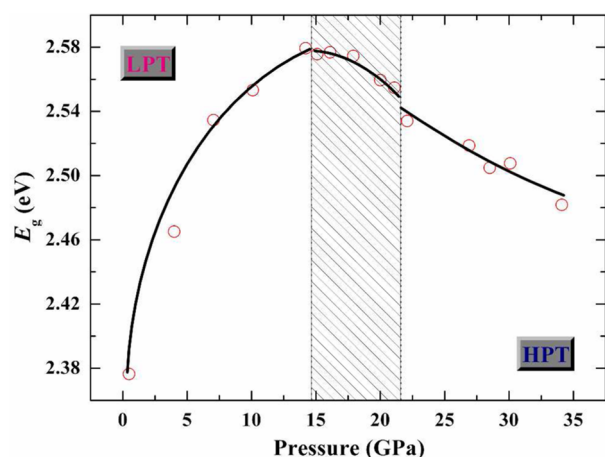


Figure 8. Pressure dependence of the band gap width (E_g) of BiOCl. The bold lines are a guide for the eyes.

this work.⁶² By the calculation without spin–orbit coupling interactions, the E_g at 0.49 GPa is equal to about 2.7 eV, which is larger than 2.38 eV when considering spin–orbit coupling interactions. Therefore, the calculation with spin–orbit coupling interactions in Bi ion could result in an underestimation of the band gap. E_g increases with increasing pressure for the LPT phase and begins to decrease at above 15.1 GPa. For the HPT phase, E_g still decreases with increasing pressure and is discontinuous at 22.1 GPa in the E_g – P relationship. In BiOX, the E_g increases with decreasing r_x , which are obtained from the calculation^{12–14} and experiment^{4–7} results, as shown in Figure S4e and S4f of the Supporting Information, respectively. So the relationship of E_g versus pressure below 14.2 GPa in BiOCl is similar to that of E_g versus decreasing r_x in BiOX. When the pressure is larger than 22.1 GPa, the evolution of E_g upon compression is different from that of the LPT phase in BiOCl and the E_g – r_x relationship in BiOX. Therefore, according to the above-mentioned experiment and calculation results, the crystal and electronic structure evolution processes upon compression of the HPT phase of BiOCl are different from those of the LPT phase.

Pressure-induced isostructural phase transition could also be found in other compounds, e.g., BiMn_2O_5 ,⁶³ Sb_2Te_3 ,⁶⁴ $\beta\text{-Bi}_2\text{O}_3$,⁶⁵ $\alpha\text{-Bi}_2\text{Te}_3$,^{66–68} $\text{Bi}_{14}\text{CrO}_{24}$,⁶⁹ PbCrO_4 ,⁷⁰ $\alpha\text{-Sb}_2\text{O}_3$,^{71,72} and so on. For bismuth compounds $\beta\text{-Bi}_2\text{O}_3$ and $\alpha\text{-Bi}_2\text{Te}_3$, the pressure dependences of the a - and c -axes are continuous, but the c/a shows a discontinuous kink at about 2 GPa.^{65–67} In Bi_2Te_3 , the isostructural phase transition upon compression is caused by the electronic topological transition (ETT) from the experimental⁶⁶ and calculated⁶⁸ results. However, in BiOCl, the a - and c -axes are discontinuous at the phase transition pressure, i.e., 15.1 GPa, which is different from that in Bi_2Te_3 . In addition, there is a transitional region between the low-pressure and high-pressure phases in BiOCl, which is the other difference in the structure evolution between it and Bi_2Te_3 . So the phase transition mechanism under high pressure in BiOCl should not be same as that in Bi_2Te_3 . From the band structures of BiOCl in Figure 7a, the highest valence bands show one maximum (M_x) at around the X high-symmetry point. With increasing pressure, the M_x shifts to the lower energy level and reaches its minimum of -0.13 eV at 15.1 GPa and then turns back to the higher energy level when the pressure is larger than 15.1 GPa. The pressure dependence of

this band maximum in BiOCl is different from that in Bi_2Te_3 , in which it still shifts to the lower energy level after the isostructural phase transition.⁶⁸ A hypothetical Fermi energy (E'_F) of -0.13 eV is plotted in the M_x at 15.1 GPa in Figure 7, being marked with the orange line. When the M_x reaches the E'_F at 15.1 GPa, the DOS near E'_F will redistribute, which could induce an ETT. Usually, an ETT can lead to anomalies in electrical, mechanical, and thermodynamic properties and then result in an isostructural phase transition. However, if the ETT happens at 15.1 GPa and causes a crystal structure phase transition in BiOCl, the hole concentration value should be equal to about $2.0 \times 10^{21} \text{ cm}^{-3}$ corresponding to the E'_F at -0.13 eV in the pressure range of 0.49 to 34.1 GPa. This concentration is too large to dope the hole in the BiOCl sample, so the isostructural phase transition at 15.1 GPa cannot be caused by an ETT. While, as the above-mentioned analyses, the redistribution of Bader charge is not related to the doping level and induces an unusual structure phase transition in BiOCl under high pressure. Then the isostructural phase transition results in abnormal DOS and band structures upon compression.

In the isostructural phase transition of the other above-mentioned compounds,^{63–72} the a -, b -, and c -axes decrease with increasing pressure in the phase transition process, which is different from the pressure dependences of a - and c -axes in BiOCl. On the other hand, their crystal structures at ambient conditions are different from that of BiOCl. So there is a difference between them and BiOCl in the compression behavior. According to the previous discussions, the structure evolution of BiOCl under high pressure is similar to that in the iron-based superconductors, rather than to the other bismuth compounds. The structure evolution with increasing a -axis and decreasing c -axis upon compression is a typical characteristic in the pressure-induced phase transitions for iron-based superconductors and other similar compounds.^{27–36} In the isostructural phase transition of BiOCl, the increasing a -axis and decreasing c -axis at the transition pressure are similar to those in the structural evolution of iron-based superconductors under high pressure. Therefore, considering the similar ambient crystal structure and similar compression behavior, the structure evolution in BiOCl could be a reference to that in the iron-based superconductors. The theoretical study results also indicate that the iron-based superconductors undergo an isostructural phase transition under high pressure.^{73–78} Taking into account the similar crystal lattice at ambient conditions and the structure evolution process upon compression, the redistribution of charge under high pressure may be a reason for the isostructural phase transition in the iron-based superconductors. However, the corresponding Bader charge calculation results are absent in the pressure dependences of crystal structure for the iron-based superconductors. So it is necessary to perform further theoretical and experimental investigations to reveal the mechanism of this special structural phase transition under high pressure. The pressure dependences of crystal and electronic structure in BiOCl can be an effective reference to the compression behaviors in the iron-based superconductors. On the other hand, correlative investigations on the other bismuth oxyhalides BiOF, BiOBr, and BiOI are important to enhance the understanding of compressed behavior for these compounds. They may also go through similar structural phase transitions under high pressure to BiOCl, due to the same crystal structure at ambient conditions. Previous calculation results showed that BiOF

exhibits three first-order structural phase transitions under high pressure,⁷⁹ without any experimental support in their work. Considering the similar crystal and electronic structure evolution processes upon compression in the LPT phase of BiOCl to those with decreasing r_x in BiOX, we plan to perform further high-pressure investigations on the BiOX series, to obtain more knowledge about these compounds and other related materials under high pressure.

CONCLUSIONS

In situ high-pressure angle-dispersive X-ray diffraction experiments at room temperature and the first-principle calculations were performed on semiconductor photocatalyst BiOCl. In the compression process, a tetragonal to tetragonal isostructural phase transition was observed at 15.1 GPa. BiOCl completely transforms into the high-pressure phase at pressures above 22.1 GPa, with discontinuous structure parameters in the transitional region of 15.1–21.1 GPa. The redistribution of Bader charge between Bi, O, Cl ions under high pressure induces this isostructural phase transition, according to the ab initio calculation results. The crystal and electronic structure evolution processes of the HPT phase of BiOCl are different from those of the LPT phase. These high-pressure structural transition behaviors in BiOCl are helpful for us to understand the structural evolution and physical property patterns for the other similar compounds upon compression.

ASSOCIATED CONTENT

Supporting Information

The Supporting Information is available free of charge on the ACS Publications website at DOI: 10.1021/acs.jpcc.5b07180.

The atomic coordination parameters at different pressures (Table S1), all the angle-dispersive X-ray diffraction patterns of BiOCl (Figure S1), the refinements of X-ray diffraction patterns of BiOCl (Figure S2), the schematic views of crystal structure evolution (Figure S3), the structural parameters and band gap width of BiOX (X = F, Cl, Br, I) (Figure S4), the band structure of BiOCl (Figure S5), the density of states of BiOCl (Figure S6), and the complete author list for refs 10, 24, 27, 29, 30, 32, 35, and 36 (PDF)

AUTHOR INFORMATION

Corresponding Authors

*Phone: +86/451/86403249. E-mail: zhaojingeng@163.com.

*E-mail: yw@hit.edu.cn.

*E-mail: liuzhiguo@hit.edu.cn.

Author Contributions

The manuscript was written through contributions of all authors. All authors have given approval to the final version of the manuscript.

Notes

The authors declare no competing financial interests.

ACKNOWLEDGMENTS

The main in situ high-pressure experiments on BiOCl were performed at the BL15U1 beamline of the Shanghai Synchrotron Radiation Facility (SSRF). Use of the National Synchrotron Light Source is supported by the U.S. Department of Energy (DOE), Office of Science, Office of Basic Energy Sciences, under contract no. DE-AC02-98CH10886. The X17C

beamline is supported by the Consortium for Materials Properties Research in Earth Sciences (COMPRES). We also thank the High Performance Computing Center of Harbin Institute of Technology for the calculation resource, and the support by the National Natural Science Foundation of China (grant no. 11274081, 10904022, 10904024), the Natural Science Foundation of Heilongjiang Province (grant no. A2015005), the Postdoctoral Science-research Developmental Foundation of Heilongjiang Province (grant no. LBH-Q12095), and the Fundamental Research Funds for the Central Universities (grant no. HIT.NSRIF.2013054).

REFERENCES

- (1) Hoffmann, M. R.; Martin, S. T.; Choi, W. Y.; Bahnemann, D. W. Environmental Applications of Semiconductor Photocatalysis. *Chem. Rev.* **1995**, *95*, 69–96.
- (2) Shenawi-Khalil, S.; Uvarov, V.; Kritsman, Y.; Menes, E.; Popov, I.; Sasson, Y. A New Family of BiO(Cl_xBr_{1-x}) Visible Light Sensitive Photocatalysts. *Catal. Commun.* **2011**, *12*, 1136–1141.
- (3) Yu, J. H.; Wei, B.; Zhu, L.; Gao, H.; Sun, W. J.; Xu, L. L. Flowerlike C-doped BiOCl Nanostructures: Facile Wet Chemical Fabrication and Enhanced UV Photocatalytic Properties. *Appl. Surf. Sci.* **2013**, *284*, 497–502.
- (4) Zhang, X.; Ai, Z. H.; Jia, F. L.; Zhang, L. Z. Generalized One-Pot Synthesis, Characterization, and Photocatalytic Activity of Hierarchical BiOX (X = Cl, Br, I) Nanoplate Microspheres. *J. Phys. Chem. C* **2008**, *112*, 747–753.
- (5) Deng, Z. T.; Chen, D.; Peng, B.; Tang, F. Q. From Bulk Metal Bi to Two-Dimensional Well-Crystallized BiOX (X = Cl, Br) Micro- and Nanostructures: Synthesis and Characterization. *Cryst. Growth Des.* **2008**, *8*, 2995–3003.
- (6) Wang, W. D.; Huang, F. Q.; Lin, X. P. xBiOI–(1-x)BiOCl as Efficient Visible-Light-Driven Photocatalysts. *Scripta Mater.* **2007**, *56*, 669–672.
- (7) Wang, W. D.; Huang, F. Q.; Lin, X. P.; Yang, J. H. Visible-Light-Responsive Photocatalysts xBiOBr–(1-x)BiOI. *Catal. Commun.* **2008**, *9*, 8–12.
- (8) Briand, G. G.; Burford, N. Bismuth Compounds and Preparations with Biological or Medicinal Relevance. *Chem. Rev.* **1999**, *99*, 2601–2658.
- (9) Kijima, N.; Matano, K.; Saito, M.; Oikawa, T.; Konishi, T.; Yasuda, H.; Sato, T.; Yoshimura, Y. Oxidative Catalytic Cracking of n-Butane to Lower Alkenes over Layered BiOCl catalyst. *Appl. Catal., A* **2001**, *206*, 237–244.
- (10) Zhang, K.; Liang, J.; Wang, S.; Liu, J.; Ren, K. X.; Zheng, X.; Luo, H.; Peng, Y. J.; Zou, X.; Bo, X.; et al. BiOCl Sub-Microcrystals Induced by Citric Acid and Their High Photocatalytic Activities. *Cryst. Growth Des.* **2011**, *12*, 793–803.
- (11) Chen, L.; Huang, R.; Xiong, M.; Yuan, Q.; He, J.; Jia, J.; Yao, M.-Y.; Luo, S.-L.; Au, C.-T.; Yin, S.-F. Room-Temperature Synthesis of Flower-like BiOX (X = Cl, Br, I) Hierarchical Structures and Their Visible-Light Photocatalytic Activity. *Inorg. Chem.* **2013**, *52*, 11118–11125.
- (12) Huang, W. L. Electronic Structures and Optical Properties of BiOX (X = F, Cl, Br, I) via DFT Calculations. *J. Comput. Chem.* **2009**, *30*, 1882–1891.
- (13) Zhao, Z. Y.; Dai, W. W. Structural, Electronic, and Optical Properties of Eu-Doped BiOX (X = F, Cl, Br, I): A DFT+U Study. *Inorg. Chem.* **2014**, *53*, 13001–13011.
- (14) Zhao, L. J.; Zhang, X. C.; Fan, C. M.; Liang, Z. H.; Han, P. D. First-Principles Study on the Structural, Electronic and Optical Properties of BiOX (X = Cl, Br, I) Crystals. *Physica B* **2012**, *407*, 3364–3370.
- (15) Soubeyrou, J. L.; Matar, S. F.; Reau, J. M.; Hagenmuller, P. Etude des Proprietes Structurales et Electriques de la Solution Solide Pb_{1-x}Bi_xO_xF_{2-x}. *Solid State Ionics* **1984**, *14*, 337–345.
- (16) Keramidis, K. G.; Voutsas, G. P.; Rentzeperis, P. I. The Crystal Structure of BiOCl. *Z. Kristallogr. - Cryst. Mater.* **1993**, *205*, 35–40.

- (17) Ketterer, J.; Kraemer, V. Structure Refinement of Bismuth Oxide Bromide, BiOBr. *Acta Crystallogr., Sect. C: Cryst. Struct. Commun.* **1986**, *42*, 1098–1099.
- (18) Keller, E.; Kraemer, V. A Strong Deviation from Vegard's Rule: X-ray Powder Investigations of the Three Quasi-Binary Systems BiOX–BiOY (X, Y = Cl, Br, I). *Z. Naturforsch., B* **2005**, *60*, 1255–1263.
- (19) Wang, X. C.; Liu, Q. Q.; Lv, Y. X.; Gao, W. B.; Yang, L. X.; Yu, R. C.; Li, F. Y.; Jin, C. Q. The Superconductivity at 18 K in LiFeAs System. *Solid State Commun.* **2008**, *148*, 538–540.
- (20) Tapp, J. H.; Tang, Z.; Lv, B.; Sasmal, K.; Lorenz, B.; Chu, P. C. W.; Guloy, A. M. LiFeAs: An Intrinsic FeAs-Based Superconductor with $T_c = 18$ K. *Phys. Rev. B: Condens. Matter Mater. Phys.* **2008**, *78*, 060505.
- (21) Pitcher, M. J.; Parker, D. R.; Adamson, P.; Herkelrath, J. C.; Boothroyd, A. T.; Ibberson, R. M.; Brunelli, M.; Clarke, S. J. Structure, Antiferromagnetism and Superconductivity of the Layered Iron Arsenide NaFeAs. *Chem. Commun.* **2008**, *45*, 5918–5920.
- (22) Kamihara, Y.; Watanabe, T.; Hirano, M.; Hosono, H. Iron-Based Layered Superconductor $\text{La}[\text{O}_{1-x}\text{F}_x]\text{FeAs}$ ($x = 0.05\text{--}0.12$) with $T_c = 26$ K. *J. Am. Chem. Soc.* **2008**, *130*, 3296–3297.
- (23) Chen, X. H.; Wu, T.; Wu, G.; Liu, R. H.; Chen, H.; Fang, D. F. Superconductivity at 43 K in $\text{SmFeAsO}_{1-x}\text{F}_x$. *Nature* **2008**, *453*, 761–762.
- (24) Ren, Z.-A.; Yang, J.; Lu, W.; Yi, W.; Shen, X.-L.; Li, Z.-C.; Che, G.-C.; Dong, X.-L.; Sun, L.-L.; Zhou, F.; et al. Superconductivity in Iron-Based F-doped Layered Quaternary Compound $\text{Nd}[\text{O}_{1-x}\text{F}_x]\text{FeAs}$. *Europhys. Lett.* **2008**, *82*, 57002.
- (25) Chen, G. F.; Li, Z.; Wu, D.; Li, G.; Hu, W. Z.; Dong, J.; Zheng, P.; Luo, J. L.; Wang, N. L. Superconductivity at 41 K and Its Competition with Spin-Density-Wave Instability in Layered $\text{CeO}_{1-x}\text{F}_x\text{FeAs}$. *Phys. Rev. Lett.* **2008**, *100*, 247002.
- (26) Chen, G. F.; Li, Z.; Wu, D.; Dong, J.; Li, G.; Hu, W. Z.; Zheng, P.; Luo, J. L.; Wang, N. L. Element Substitution Effect in Transition Metal Oxypnictide $\text{Re}(\text{O}_{1-x}\text{F}_x)\text{TAs}$ (Re = Rare Earth, T = Transition Metal). *Chin. Phys. Lett.* **2008**, *25*, 2235–2238.
- (27) Zhao, J. G.; Wang, L. H.; Dong, D. W.; Liu, Z. G.; Liu, H. Z.; Chen, G. F.; Wu, D.; Luo, J. L.; Wang, N. L.; Yu, Y.; et al. Structure Stability and Compressibility of Iron-based Superconductor $\text{Nd}(\text{O}_{0.88}\text{F}_{0.12})\text{FeAs}$ under High Pressure. *J. Am. Chem. Soc.* **2008**, *130*, 13828–13829.
- (28) Zhao, J. G.; Liu, H. Z.; Ehm, L.; Dong, D. W.; Chen, Z. Q.; Liu, Q. Q.; Hu, W. Z.; Wang, N. L.; Jin, C. Q. Pressure-Induced Phase Transitions and Correlation between Structure and Superconductivity in Iron-Based Superconductor $\text{Ce}(\text{O}_{0.84}\text{F}_{0.16})\text{FeAs}$. *Inorg. Chem.* **2013**, *52*, 8067–8073.
- (29) Kreyssig, A.; Green, M. A.; Lee, Y.; Samolyuk, G. D.; Zajdel, P.; Lynn, J. W.; Bud'ko, S. L.; Torikachvili, M. S.; Ni, N.; Nandi, S.; et al. Pressure-Induced Volume-Collapsed Tetragonal Phase of CaFe_2As_2 as Seen via Neutron Scattering. *Phys. Rev. B: Condens. Matter Mater. Phys.* **2008**, *78*, 184517.
- (30) Mittal, R.; Heid, R.; Bosak, A.; Forrest, T. R.; Chaplot, S. L.; Lamago, D.; Reznik, D.; Bohnen, K.-P.; Su, Y.; Kumar, N.; et al. Pressure Dependence of Phonon Modes across the Tetragonal to Collapsed-Tetragonal Phase Transition in CaFe_2As_2 . *Phys. Rev. B: Condens. Matter Mater. Phys.* **2010**, *81*, 144502.
- (31) Uhoya, W. O.; Montgomery, J. M.; Tsoi, G. M.; Vohra, Y. K.; McGuire, M. A.; Sefat, A. S.; Sales, B. C.; Weir, S. T. Phase Transition and Superconductivity of SrFe_2As_2 under High Pressure. *J. Phys.: Condens. Matter* **2011**, *23*, 122201.
- (32) Mittal, R.; Mishra, S. K.; Chaplot, S. L.; Ovsyannikov, S. V.; Greenberg, E.; Trots, D. M.; Dubrovinsky, L.; Su, Y.; Brueckel, Th.; Matsuishi, S.; et al. Ambient- and Low-Temperature Synchrotron X-ray Diffraction Study of BaFe_2As_2 and CaFe_2As_2 at High Pressures up to 56 GPa. *Phys. Rev. B: Condens. Matter Mater. Phys.* **2011**, *83*, 054503.
- (33) Uhoya, W.; Stemshorn, A.; Tsoi, G.; Vohra, Y. K.; Sefat, A. S.; Sales, B. C.; Hope, K. M.; Weir, S. T. Collapsed Tetragonal Phase and Superconductivity of BaFe_2As_2 under High Pressure. *Phys. Rev. B: Condens. Matter Mater. Phys.* **2010**, *82*, 144118.
- (34) Uhoya, W.; Tsoi, G.; Vohra, Y. K.; McGuire, M. A.; Sefat, A. S.; Sales, B. C.; Mandrus, D.; Weir, S. T. Anomalous Compressibility Effects and Superconductivity of EuFe_2As_2 under High Pressures. *J. Phys.: Condens. Matter* **2010**, *22*, 292202.
- (35) Yu, Z. H.; Wang, L.; Wang, L. H.; Liu, H. Z.; Zhao, J. G.; Li, C. Y.; Sinogeikin, S.; Wu, W.; Luo, J. L.; Wang, N. L.; et al. Conventional Empirical Law Reverses in the Phase Transitions of 122-type Iron-Based Superconductors. *Sci. Rep.* **2014**, *4*, 7172.
- (36) Liu, Q. Q.; Yu, X. H.; Wang, X. C.; Deng, Z.; Lv, Y. X.; Zhu, J. L.; Zhang, S. J.; Liu, H. Z.; Yang, W. G.; Wang, L.; et al. Pressure-Induced Isostructural Phase Transition and Correlation of FeAs Coordination with the Superconducting Properties of 111-Type $\text{Na}_{1-x}\text{FeAs}$. *J. Am. Chem. Soc.* **2011**, *133*, 7892–7896.
- (37) Zhang, Y. Z.; Jeschke, H. O.; Valentí, R. Two Pressure-Induced Transitions in TiOCl: Mott Insulator to Anisotropic Metal. *Phys. Rev. Lett.* **2008**, *101*, 136406.
- (38) Blanco-Canosa, S.; Rivadulla, F.; Piñeiro, A.; Pardo, V.; Baldomir, D.; Khomskii, D. I.; Abd-Elmeguid, M. M.; López-Quintela, M. A.; Rivas, J. Enhanced Dimerization of TiOCl under Pressure: Spin-Peierls to Peierls Transition. *Phys. Rev. Lett.* **2009**, *102*, 056406.
- (39) Ebad-Allah, J.; Schönleber, A.; van Smaalen, S.; Hanfland, M.; Klemm, M.; Horn, S.; Glawion, S.; Sing, M.; Claessen, R.; Kuntscher, C. A. Two Pressure-Induced Structural Phase Transitions in TiOCl. *Phys. Rev. B: Condens. Matter Mater. Phys.* **2010**, *82*, 134117.
- (40) Forthaus, M. K.; Taetz, T.; Möller, A.; Abd-Elmeguid, M. M. Effect of Pressure on the Electrical Transport and Structure of TiOCl. *Phys. Rev. B: Condens. Matter Mater. Phys.* **2008**, *77*, 165121.
- (41) Kuntscher, C. A.; Frank, S.; Pashkin, A.; Hoinkne, M.; Klemm, M.; Sing, M.; Horn, S.; Claessen, R. Possible Pressure-Induced Insulator-to-Metal Transition in Low-Dimensional TiOCl. *Phys. Rev. B: Condens. Matter Mater. Phys.* **2006**, *74*, 184402.
- (42) Mao, H. K.; Xu, J. A.; Bell, P. M. Calibration of the Ruby Pressure Gauge to 800 kbar under Quasi-Hydrostatic Conditions. *J. Geophys. Res.* **1986**, *91*, 4673–4676.
- (43) Shen, Y. R.; Kumar, R. S.; Pravica, M.; Nicol, M. F. Characteristics of Silicone Fluid as a Pressure Transmitting Medium in Diamond Anvil Cells. *Rev. Sci. Instrum.* **2004**, *75*, 4450–4454.
- (44) You, S. J.; Chen, L. C.; Jin, C. Q. Hydrostaticity of Pressure Media in Diamond Anvil Cells. *Chin. Phys. Lett.* **2009**, *26*, 096202.
- (45) Errandonea, D.; Meng, Y.; Somayazulu, M.; Häusermann, D. Pressure-Induced $\alpha \rightarrow \omega$ Transition in Titanium Metal: A Systematic Study of the Effects of Uniaxial Stress. *Physica B* **2005**, *355*, 116–125.
- (46) Klotz, S.; Chervin, J.-C.; Munsch, P.; Le Marchand, G. Hydrostatic Limits of 11 Pressure Transmitting Media. *J. Phys. D: Appl. Phys.* **2009**, *42*, 075413.
- (47) Errandonea, D.; Muñoz, A.; Gonzalez-Platas, J. Comment on “High-pressure X-ray Diffraction Study of $\text{YBO}_3/\text{Eu}^{3+}$, GdBO_3 , and EuBO_3 : Pressure-Induced Amorphization in GdBO_3 ” [J. Appl. Phys. **115**, 043507 (2014)]. *J. Appl. Phys.* **2014**, *115*, 216101.
- (48) Hammersley, A. P.; Svensson, S. O.; Hanfland, M.; Fitch, A. N.; Häusermann, D. Two-Dimensional Detector Systems: From Real Detector to Idealised Image of Two-theta Scan. *High Pressure Res.* **1996**, *14*, 235–248.
- (49) Rietveld, H. M. Line Profiles of Neutron Powder-Diffraction Peaks for Structure Refinement. *Acta Crystallogr.* **1967**, *22*, 151–152.
- (50) Larson, A. C.; Von Dreele, R. B. *General Structure Analysis System (GSAS)*, Los Alamos National Laboratory, Report LAUR 86-748; Los Alamos National Laboratory: Los Alamos, NM, 1994.
- (51) Toby, B. H. EXPGUI, A Graphical User Interface for GSAS. *J. Appl. Crystallogr.* **2001**, *34*, 210–213.
- (52) Kraus, W.; Nolze, G. POWDER CELL - A Program for the Representation and Manipulation of Crystal Structures and Calculation of the Resulting X-Ray Powder Patterns. *J. Appl. Crystallogr.* **1996**, *29*, 301–303.

- (53) Tang, W.; Sanville, E.; Henkelman, G. A. Grid-Based Bader Analysis Algorithm without Lattice Bias. *J. Phys.: Condens. Matter* **2009**, *21*, 084204.
- (54) Blöchl, P. E. Projector Augmented-Wave Method. *Phys. Rev. B: Condens. Matter Mater. Phys.* **1994**, *50*, 17953–17979.
- (55) Kresse, G.; Furthmüller, J. Efficient Iterative Schemes for ab initio Total-Energy Calculations Using a Plane-Wave Basis Set. *Phys. Rev. B: Condens. Matter Mater. Phys.* **1996**, *54*, 11169–11186.
- (56) Perdew, J. P.; Burke, K.; Ernzerhof, M. Generalized Gradient Approximation Made Simple. *Phys. Rev. Lett.* **1996**, *77*, 3865–3868.
- (57) Birch, F. Finite Elastic Strain of Cubic Crystals. *Phys. Rev.* **1947**, *71*, 809–824.
- (58) Angel, R. J. Equation of State. *Rev. Mineral. Geochem.* **2000**, *41*, 35–59.
- (59) Angel, R. J.; Gonzalez-Platas, J.; Alvaro, M. EosFit7c and a Fortran Module (Library) for Equation of State Calculations. *Z. Kristallogr. - Cryst. Mater.* **2014**, *229*, 405–419.
- (60) Errandonea, D.; Gomis, O.; Santamaría-Perez, D.; García-Domene, B.; Muñoz, A.; Rodríguez-Hernández, P.; Achary, S. N.; Tyagi, A. K.; Popescu, C. Exploring the High-Pressure Behavior of the Three Known Polymorphs of BiPO₄: Discovery of a New Polymorph. *J. Appl. Phys.* **2015**, *117*, 105902.
- (61) Errandonea, D.; Popescu, C.; Achary, S. N.; Tyagi, A. K.; Bettinelli, M. In Situ High-Pressure Synchrotron X-ray Diffraction Study of the Structural Stability in NdVO₄ and LaVO₄. *Mater. Res. Bull.* **2014**, *50*, 279–284.
- (62) Shannon, R. D. Revised Effective Ionic Radii and Systematic Studies of Interatomic Distances in Halides and Chalcogenides. *Acta Crystallogr., Sect. A: Cryst. Phys., Diffr., Theor. Gen. Crystallogr.* **1976**, *A32*, 751–767.
- (63) Pandey, K. K.; Poswal, H. K.; Kumar, R.; Sharma, S. M. High Pressure Iso-structural Phase Transition in BiMn₂O₅. *J. Phys.: Condens. Matter* **2013**, *25*, 325401.
- (64) Zhao, K.; Wang, Y.; Sui, Y.; Xin, C.; Wang, X. J.; Wang, Y.; Liu, Z. G.; Li, B. S. First Principles Study of Isostructural Phase Transition in Sb₂Te₃ under High Pressure. *Phys. Status Solidi RRL* **2015**, *9*, 379–383.
- (65) Pereira, A. L. J.; Sans, J. A.; Vilaplana, R.; Gomis, O.; Manjón, F. J.; Rodríguez-Hernández, P.; Muñoz, A.; Popescu, C.; Beltrán, A. Isostructural Second-Order Phase Transition of β-Bi₂O₃ at High Pressures: An Experimental and Theoretical Study. *J. Phys. Chem. C* **2014**, *118*, 23189–23201.
- (66) Polian, A.; Gauthier, M.; Souza, S. M.; Trichês, D. M.; Cardoso de Lima, J.; Grandi, T. A. Two-Dimensional Pressure-Induced Electronic Topological Transition in Bi₂Te₃. *Phys. Rev. B: Condens. Matter Mater. Phys.* **2011**, *83*, 113106.
- (67) Nakayama, A.; Einaga, M.; Tanabe, Y.; Nakano, S.; Ishikawa, F.; Yamada, Y. Structural Phase Transition in Bi₂Te₃ under High Pressure. *High Pressure Res.* **2009**, *29*, 245–249.
- (68) Ibarra-Hernández, W.; Verstraete, M. J.; Raty, J.-Y. Effect of Hydrostatic Pressure on the Thermoelectric Properties of Bi₂Te₃. *Phys. Rev. B: Condens. Matter Mater. Phys.* **2014**, *90*, 245204.
- (69) Errandonea, D.; Santamaria-Perez, D.; Achary, S. N.; Tyagi, A. K. Experimental Evidence for Pressure-Driven Isostructural and Symmetry-Breaking Phase Transitions on Bi₄CrO₂₄. *Solid State Commun.* **2014**, *182*, 50–54.
- (70) Bandiello, E.; Errandonea, D.; Martinez-Garcia, D.; Santamaria-Perez, D.; Manjón, F. J. Effects of High-Pressure on the Structural, Vibrational, and Electronic Properties of Monazite-type PbCrO₄. *Phys. Rev. B: Condens. Matter Mater. Phys.* **2012**, *85*, 024108.
- (71) Pereira, A. L. J.; Gracia, L.; Santamaría-Pérez, D.; Vilaplana, R.; Manjón, F. J.; Errandonea, D.; Nalin, M.; Beltrán, A. Structural and Vibrational Study of Cubic Sb₂O₃ under High Pressure. *Phys. Rev. B: Condens. Matter Mater. Phys.* **2012**, *85*, 174108.
- (72) Zhao, Z.; Zeng, Q. S.; Zhang, H. J.; Wang, S. B.; Hirai, S.; Zeng, Z. D.; Mao, W. L. Structural Transition and Amorphization in Compressed α-Sb₂O₃. *Phys. Rev. B: Condens. Matter Mater. Phys.* **2015**, *91*, 184112.
- (73) Backes, S.; Jeschke, H. O. Finite Temperature and Pressure Molecular Dynamics for BaFe₂As₂. *Phys. Rev. B: Condens. Matter Mater. Phys.* **2013**, *88*, 075111.
- (74) Tomić, M.; Jeschke, H. O.; Fernandes, R. M.; Valentí, R. In-Plane Uniaxial Stress Effects on the Structural and Electronic Properties of BaFe₂As₂ and CaFe₂As₂. *Phys. Rev. B: Condens. Matter Mater. Phys.* **2013**, *87*, 174503.
- (75) Tomić, M.; Valentí, R.; Jeschke, H. O. Uniaxial versus Hydrostatic Pressure-Induced Phase Transitions in CaFe₂As₂ and BaFe₂As₂. *Phys. Rev. B: Condens. Matter Mater. Phys.* **2012**, *85*, 094105.
- (76) Mandal, S.; Cohen, R. E.; Haule, K. Pressure Suppression of Electron Correlation in the Collapsed Tetragonal Phase of CaFe₂As₂: A DFT-DMFT Investigation. *Phys. Rev. B: Condens. Matter Mater. Phys.* **2014**, *90*, 060501.
- (77) Xie, W. H.; Bao, M. L.; Zhao, Z. J.; Liu, B. G. First-Principles Investigation of the Effect of Pressure on BaFe₂As₂. *Phys. Rev. B: Condens. Matter Mater. Phys.* **2009**, *79*, 115128.
- (78) Zhang, X. X.; Wang, Y. C.; Ma, Y. M. High Pressure Structures of “111” Type Iron-Based Superconductors Predicted from First-Principles. *Phys. Chem. Chem. Phys.* **2012**, *14*, 15029–15035.
- (79) Zhou, D. W.; Pu, C. Y.; He, C. Z.; Zhang, F. W.; Lu, C.; Bao, G. Pressure-Induced Phase Transition of BiOF: Novel Two-Dimensional Layered Structures. *Phys. Chem. Chem. Phys.* **2015**, *17*, 4434–4440.